JACS
JOURNAL OF THE AMERICAN CHEMICAL SOCIETY
Article
pubs.acs.org/JACS

Strong Facet-Induced and Light-Controlled Room-Temperature Ferromagnetism in Semiconducting β-$FeSi_2$ Nanocubes

Zhiqiang He, Shijie Xiong, Shuyi Wu, Xiaobin Zhu, Ming Meng, and Xinglong Wu*

Key Laboratory of Modern Acoustics, MOE, Institute of Acoustics, Collaborative Innovation Center of Advanced Microstructures, National Laboratory of Solid State Microstructures, Nanjing University, Nanjing 210093, P. R. China

Supporting Information

ABSTRACT: Crystalline β-$FeSi_2$ nanocubes with two {100} facets and four {011} lateral facets synthesized by spontaneous one-step chemical vapor deposition exhibit strong room-temperature ferromagnetism with saturation magnetization of 15 emu/g. The room-temperature ferromagnetism is observed from the β-$FeSi_2$ nanocubes larger than 150 nm with both the {100} and {011} facets. The ferromagnetism is tentatively explained with a simplified model including both the itinerant electrons in surface states and the local moments on Fe atoms near the surfaces. The work demonstrates the transformation from a nonmagnetic semiconductor to a magnetic one by exposing specific facets and the room-temperature ferromagnetism can be manipulated under light irradiation. The semiconducting β-$FeSi_2$ nanocubes may have large potential in silicon-based spintronic applications.

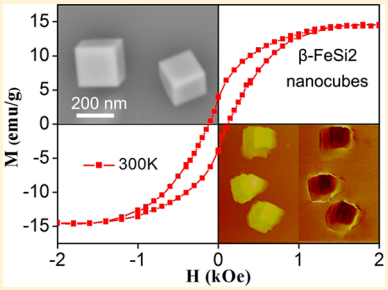

INTRODUCTION

Spintronics has attracted much research interest because of potential improvement in the performance of solid-state electronic and photonic devices[1−3] and in particular, diluted magnetic semiconductors and oxides, in which magnetism can be induced by various methods,[4−8] are studied extensively. However, the origin of ferromagnetism remains controversial and only weak magnetism can be achieved because of the small solubility of magnetic dopants, for example, manganese in GaAs.[4] It is of both scientific and technological significance to obtain strong and stable ferromagnetism with a high Curie temperature.[9,10]

As an environmentally friendly semiconductor, beta-phase iron disilicide (β-$FeSi_2$) has been widely investigated in optoelectronics and photovoltaic applications.[11−14] There are several techniques to fabricate β-$FeSi_2$, for instance, ion beam synthesis,[15] reactive deposition epitaxy,[16] magnetron sputtering,[17] molecular beam epitaxy,[18] chemical vapor deposition (CVD),[19,20] and high-temperature reduction in a solution phase[21] and most of the previous studies have focused on the fabrication of thin films or nanoparticles. β-$FeSi_2$ samples without magnetic dopants prepared by powder metallurgy show diamagnetism at low temperature[22] and Hall effect measurements of β-$FeSi_2$ polycrystalline films reveal that ferromagnetism is attained only at a temperature below 100 K.[23] The saturation magnetization values of both n-type and p-type β-$FeSi_2$[24,25] are also quite small (1×10^{-3} emu/g).[26] Ni- or Cr-doped β-$FeSi_2$ single crystals have been reported to have small saturation magnetization at different temperature but there is a ferromagnetic signature at a low temperature.[27] Although β-$FeSi_2$ nanowires have been shown to have ferromagnetic behavior even at the room temperature (1×10^{-3} emu),[19,28] the origin is unclear. Nanoparticles of $FeSi_2$ exhibit superparamagnetism.[29] The relatively low saturation magnetization suggests that the magnetic behavior is associated with only a small fraction of Fe ions. From density functional calculations, Singh and Parker predicted Stoner itinerant magnetism in doped β-$FeSi_2$.[30]

Herein, a facet-cutting technique is employed to synthesize crystalline semiconducting β-$FeSi_2$ nanocubes via one-step spontaneous CVD and strong room-temperature ferromagnetism is observed from the β-$FeSi_2$ nanocubes larger than 150 nm with both the {100} and {011} facets. The strong ferromagnetism can be manipulated with light irradiation. The semiconducting nanomagnets may have large potential in spintronic devices as well as magneto-optic components.

RESULTS AND DISCUSSION

The β-$FeSi_2$ nanocubes are prepared in a CVD system by precisely controlling the flow rate and temperature (Figure S1). As shown in Figure 1a, there are many cubic particles with dimensions between 200 and 400 nm on the single crystal Si substrate. The magnified image in the inset clearly shows that the nanocubes have sharp edges and smooth surfaces. Figure 1b depicts the scanning electron microscopy (SEM) image of a representative nanocube particle and Figure 1c shows a simulated cube. The X-ray diffraction (XRD) patterns acquired from the β-$FeSi_2$ nanocubes are displayed in Figure 1d. All the diffraction peaks can be indexed to the (220), (313), (331), (004), (040), and (422) reflections from the orthorhombic structure of β-$FeSi_2$ (JCPDS card 71−0642). No crystalline iron and iron oxide (Fe_3O_4 and γ-Fe_2O_3) XRD peaks can be

Received: June 23, 2015
Published: August 24, 2015

DOI: 10.1021/jacs.5b06507
J. Am. Chem. Soc. 2015, 137, 11419−11424

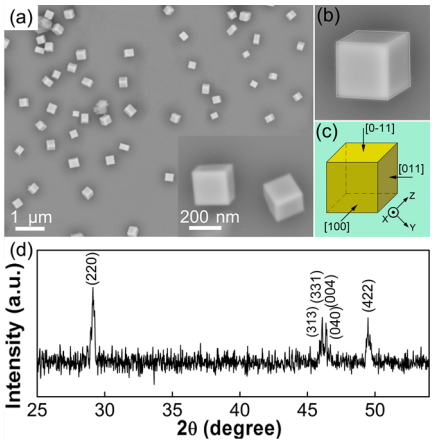

Figure 1. (a) FE-SEM image of the β-$FeSi_2$ nanocubes. Inset: magnified image of two nanocubes. (b) FE-SEM image of a representative nanocube. (c) Schematic diagram of a nanocube. (d) XRD pattern indicating that all diffraction peaks can be associated with the β-$FeSi_2$ phase with an orthorhombic structure.

observed, suggesting that these compounds are not present in the β-$FeSi_2$ nanocubes.

Figure 2a, e shows the representative low-magnification transmission electron microcopy (TEM) images of the as-synthesized β-$FeSi_2$ nanocubes along the [0−11] and [100] axes, respectively. The nanocubes have straight sides and regular ends. The selected-area electron diffraction (SAED) patterns confirm the different crystal facets shown in Figure 2b, f corresponding to Figure 2a, e. No amorphous diffusive diffraction spots can be observed suggesting that the particle is a single crystal. Figure 2b exhibits sharp diffraction spots along the [0−11] axis of the nanocube with the (022) and (400) planes, disclosing that the nanocube is a single crystal with four {011} lateral facets and two {100} top facets which will be further confirmed. Tetragonal symmetric diffraction spots along the [100] axis are shown in Figure 2f. The lattice constants of the b and c axes are very similar and the crystallographic nature of an individual β-$FeSi_2$ nanocube is further examined by high-resolution TEM (HR-TEM). Figures 2c, d are sections of the left and top edges of a β-$FeSi_2$ nanocube along the [0−11] axis illustrating that the flat sides are parallel to the (100) and (011) planes. The (011) side planes are also observed along the [100] axis (Figure 2g). The angle between the (040) plane and top edge is about 45° which agrees well with the angle between the (040) and (011) planes. A schematic illustration of the nanocube is presented in Figure 2h indicating that the β-$FeSi_2$ nanocube has two exposed {100} facets and four {011} lateral facets. Energy dispersive X-ray (EDX) spectrum shows that the sample is composed of Fe and Si and is not doped with other elements (Figure S2).

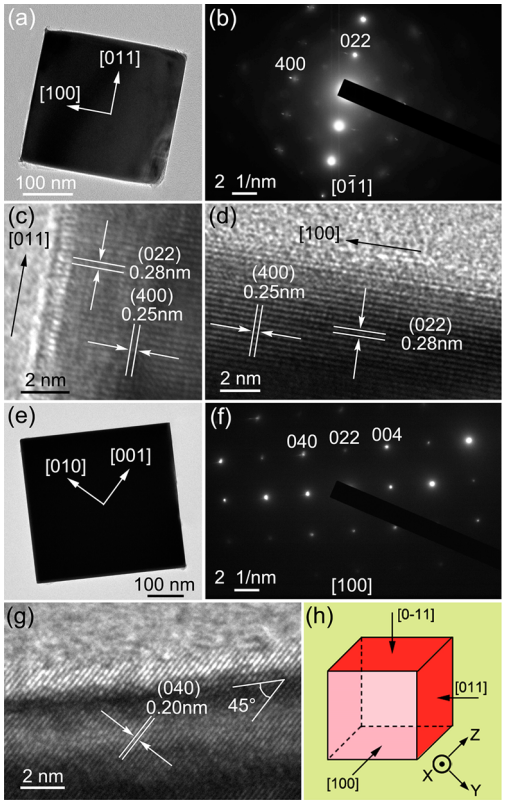

Figure 2. (a, b) Low-magnification TEM image and SAED pattern along the [0−11] axis. (c, d) HR-TEM images along the [0−11] axis. (e, f) Low-magnification TEM image and SAED pattern along the [100] axis. (g) HR-TEM image along the [100] axis. (h) Schematic illustration of the nanocube.

Formation of the β-$FeSi_2$ nanocubes from the evaporated $FeCl_2$ precursor vapor on the silicon substrate proceeds by the following reactions

$$2FeCl_2(g) + 5Si(s) \rightarrow 2\beta\text{-}FeSi_2(s) + SiCl_4(g) \quad (1)$$

$$FeCl_2(g) + 2SiCl_4(g) \rightarrow \beta\text{-}FeSi_2(s) + 5Cl_2(g) \quad (2)$$

Initially, the $FeCl_2$ vapor is transported to the downstream zone and reacts directly with the Si substrate to form β-$FeSi_2$ and $SiCl_4$. The $FeCl_2$ vapor and $SiCl_4$ produced in reaction 1 undergoes a gas phase reaction to produce the β-$FeSi_2$ nanostructure. The detailed growth and mechanism are described in Figures S3−S5.

To obtain insights into the magnetic characteristics of the β-$FeSi_2$ nanocube assembly, magnetization as a function of magnetic field (M-H) is studied on a superconducting quantum interference device (SQUID) at different temperature (Figure 3). The applied magnetic field is parallel to the Si substrate. As shown in Figure 3a, the nonlinear hysteresis loop curve suggests that the β-$FeSi_2$ nanocubes are ferromagnetic at room temperature with nonzero residual magnetization and coercivity (green line). The saturation magnetization (15 emu/g) at 300 K is strong and even comparable to the results obtained from iron-rich ferromagnetic phases such as Fe_5Si_3.[31] The inset in Figure 3a shows the temperature-dependent magnetization (M−T) curve measured by a vibrating sample magnetometer (VSM) at an applied magnetic field of 500 Oe in the temperature range between 300 and 750 K. The magnetization intensity decreases monotonically with temperature. Although we cannot determine the magnetization properties at a temperature higher than 750 K, it is inferred that the Curie temperature of the β-$FeSi_2$ nanocubes is about 800 K by extrapolating the M−T curve using mean field approximation.[32] Figure 3b shows the M−H curves at 10, 100, and 200 K. The coercive field (H_c) and residual magnetization (M_r) are found to increase with decreasing temperature due to reduced thermal fluctuation (inset). The M−H curves are obtained after subtracting the diamagnetic contribution from the substrate.

Magnetic force microscopy (MFM) images are acquired to corroborate that the room-temperature ferromagnetism stems

DOI: 10.1021/jacs.5b06507
J. Am. Chem. Soc. 2015, 137, 11419−11424

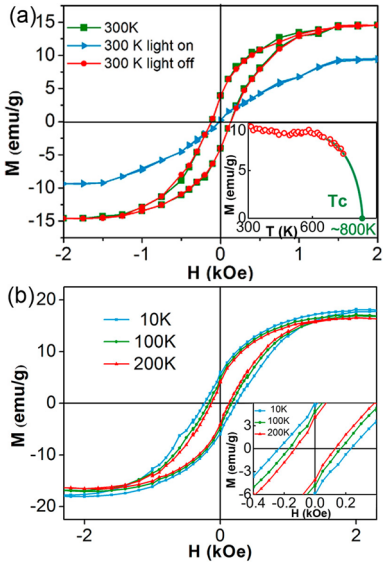

Figure 3. (a) $M-H$ curves of the β-$FeSi_2$ nanocubes measured at room temperature. The green and blue curves are the data before and under light irradiation, respectively. The red curve is the data after the light illumination is repealed. Inset: $M-T$ curve of the β-$FeSi_2$ nanocubes in the range of 300−750 K. The extrapolated line of the high temperature data intersects the temperature axis at around 800 K indicating the Curie temperature. (b) $M-H$ curves of the β-$FeSi_2$ nanocubes measured at various temperatures below room temperature. Inset: the loops on an enlarged scale.

from the β-$FeSi_2$ nanocubes. Figure 4a shows a large-area topographical picture which is consistent with the SEM picture

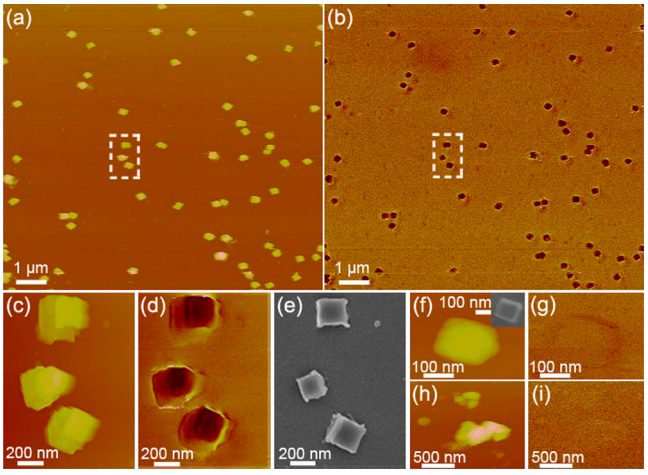

Figure 4. (a, b) Topography and MFM images of large scale nanocubes. (c, d) Details of the regions demarcated by boxes in a and b. (e) SEM image from the same site in c. (f, g) and (h, i) Topography and MFM images of smaller nanocubes and irregular particles, respectively. The inset in f shows the corresponding SEM image of this nanocube.

in Figure 1a. According to the corresponding magnetic image in Figure 4b, the magnetic domain can only be found from the β-$FeSi_2$ nanocubes. This relationship can be clearly observed from Figures 4c and 2d, which show the topography and MFM images of the regions enclosed by the boxes in Figure 4a, b. Figure 4e depicts the SEM image of three β-$FeSi_2$ nanocubes having an average size of 200 nm in the boxes. Small β-$FeSi_2$ nanocubes (<150 nm) formed by reducing the reaction time can be seen from Figure 4f and the inset, but almost no magnetic domain is observed (Figure 4g). The results suggest that room-temperature ferromagnetism depends on the size and the smallest size for this to occur is about 150 nm. In contrast, particles with an irregular shape with dimensions from 100 to 500 nm in Figure 4h,i show no magnetism at all. The morphology-dependent magnetism clearly reveals that ferromagnetism arises from the exposed specific facets of the β-$FeSi_2$ nanocubes larger than 150 nm.

As unintended impurities can influence the magnetic properties, the phase purity is studied. To determine the chemical state and relative intensity of the iron species in the sample, ^{57}Fe Mössbauer spectra are acquired at room temperature. A typical room-temperature Mössbauer spectrum is presented in Figure 5. The experimental pattern can be

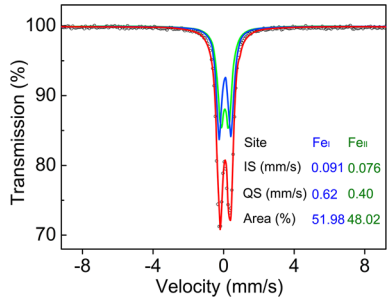

Figure 5. Mössbauer spectrum of the as-grown β-$FeSi_2$ nanocubes measured at room temperature. The fitted lines represent two quadrupole doublets (blue and green). Inset: Summary of the parameters of the two quadrupole doublets corresponding to two crystallographically nonequivalent Fe sites. The quadrupole splitting, isomer shifts, and the relative areas are given.

divided into two quadrupole doublets by considering the two crystallographically nonequivalent Fe sites in the orthorhombic β-$FeSi_2$ lattice.[33] The obtained values for the isomer shift (IS) and quadrupole splitting (QS) are given in Figure 5 and can be compared to other room-temperature data in the literature.[33] However, we do not observe any metallic iron or iron oxides as hematite, maghemite, and magnetite suggesting that the ferromagnetism primarily stems from β-$FeSi_2$.

The X-ray photoelectron spectroscopy (XPS) results are presented in Figure 6. The Si 2p, Fe 2p, and O 1s core level XPS spectra are acquired from the β-$FeSi_2$ nanocubes. In the Fe 2p spectrum (Figure 6a), in addition to the two main peaks at 707.7 and 720.6 eV, which are related to the β-$FeSi_2$ nanocube,[34] a weak shoulder peak appears at 709.4 eV as a result of oxidation of iron (FeO) on the β-$FeSi_2$ nanocube surface after exposure to air. No Fe^{3+} is detected.[35] In the Si 2p spectrum (Figure 6b), a shoulder peak is observed at 102.0 eV attributable to silicon suboxide (SiO).[36] The SiO component also appears at 532.5 eV from the O 1s spectrum (Figure 6c).[37] It can be concluded that the β-$FeSi_2$ nanocube surface has small amounts of SiO and FeO due to oxidation of Si and Fe dangling bonds and Fe clusters (or film), hematite, maghemite, and magnetite are not present in the β-$FeSi_2$ nanocubes.

To further confirm the facet-induced room-temperature ferromagnetism, MFM images were acquired from the oxidized nanocubes (Figure S6a, b) after exposing the pristine sample to dry air at room temperature for weeks. The MFM image shows that the ferromagnetism vanishes. It can be explained that Fe

DOI: 10.1021/jacs.5b06507
J. Am. Chem. Soc. 2015, 137, 11419−11424

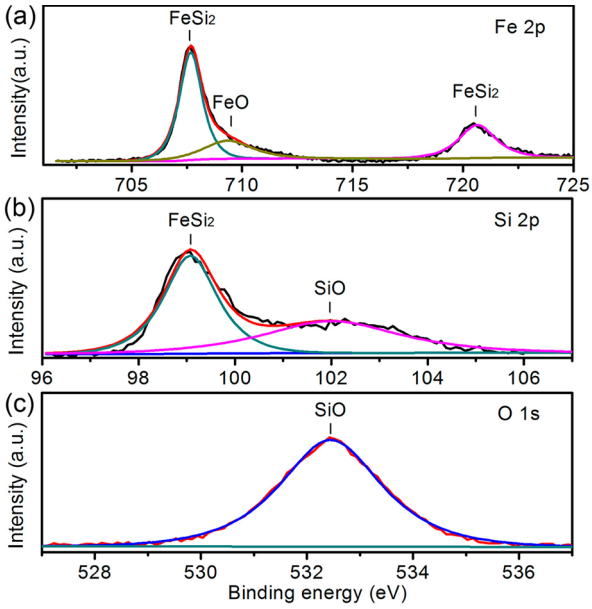

Figure 6. Core level XPS spectra acquired from the pristine (as-made) and oxidized β-$FeSi_2$ nanocubes on the Si substrate: (a) Fe 2p, (b) Si 2p, and (c) O 1s.

dangling bonds on the specific facets which induce the room-temperature ferromagnetism are terminated by oxygen. To avoid the surface oxidation and possible magnetic disappearance for practical applications, we deposited a thin layer of Au (10 nm) on the pristine β-$FeSi_2$ nanocubes before oxidization. The topography and MFM images of the Au-covered sample in Figure S6c, d are similar to those in Figure 4d, which indicates that the ferromagnetic surface can be protected adequately by a gold film.

In semiconducting silicon, the unpaired spins associated with naturally occurring dangling bonds may contribute to the magnetism.[38,39] The ferromagnetic properties can originate from the interactions between charge carriers (electrons or holes) and localized dangling bonds and they may be significant in a nanoscale system.[19,40] It has been observed that bulk diamagnetic materials become ferromagnetic as they become nanoscale ones.[40] Furthermore, the magnetic properties of nanowires depend on the crystalline orientation of the nanowires and there are contributions from both magneto-crystalline anisotropy and shape anisotropy.[41,42] However, the relationship between the lateral facets of nanowires and magnetic properties is not well understood. The strong room-temperature ferromagnetism observed from the β-$FeSi_2$ nanocubes may originate from the reduced coordination of the surface Fe atoms on both the {011} and {100} facets.

To seek the possible origin of the facet- and size-dependent ferromagnetism, first-principles calculation is carried out to determine the spin configurations on both the {011} and {100} surfaces and conditions for ferromagnetism to occur. As shown in Figure S7, on both the {011} and {100} surfaces, the moments of the Fe atoms are large and exhibit ferromagnetic arrangements, whereas in the bulk the moments are relatively small and some spins align in the opposite direction. The density of spin states and orbitals of gap states near the Fermi level for the {100} surfaces are calculated and shown in Figure 7. It can be seen that there are two surface subbands in the energy gap. One has down spin ($\sigma = -1$) and is partially

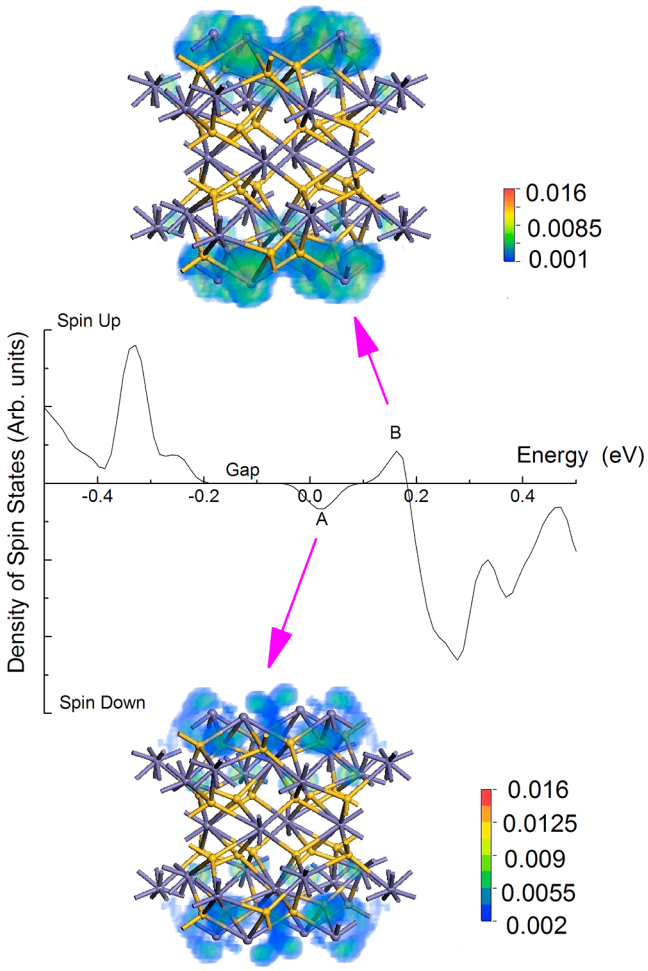

Figure 7. Densities of spin states and electron orbitals of the β-$FeSi_2$ slab in {100} direction. Middle panel, density of spin states around the gap. Peaks A and B are bands within the gap with down and up spins, respectively. Lower panel, orbitals of electrons in {100} surface states of peak A with down spin. Upper panel, orbitals of electrons in {100} surface states of peak B with up spin. Purple and yellow balls represent Fe and Si atoms, respectively.

occupied. The other has up spin ($\sigma = +1$) and is empty. They can approximately be described with the following Hamiltonian

$$H = \sum_{k,\sigma} [E_k - \mu_B h\sigma + \lambda I\langle n_{-\sigma}\rangle] c^{\dagger}_{k,\sigma} c_{k,\sigma} \quad (3)$$

where $c_{k,\sigma}$ ($c^{\dagger}_{k,\sigma}$) is the annihilation (creation) operator for electrons with state index k and spin σ, E_k is the band energy, h is the effective magnetic field, μ_B is the Bohr magneton, I is the average repulsion energy when two electrons are on a same site, $\langle n_\sigma\rangle$ is the average number of electrons with spin σ of a site, and λ is a factor taking into account the effect of nanocube edges on surface itinerant electrons. The magnetic interaction between itinerant electrons and local magnetic moments S is included in the effective field as $h = h_0 + JS\langle \cos\theta\rangle$, where h_0 is the external magnetic field, J is the average interaction strength, and $\langle \cos\theta\rangle$ is the average direction cosine between local moments and external field. With several adjustable parameters, the magnetization and the Curie temperature can be calculated (Supporting Information) and shown in Figure 8. The calculations present a possible explanation for the experimental results.

DOI: 10.1021/jacs.5b06507
J. Am. Chem. Soc. 2015, 137, 11419−11424

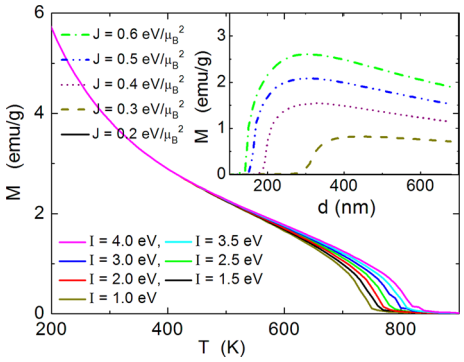

Figure 8. Main panel: Calculated temperature dependence of magnetization of the surface Fe atoms. The parameters are $\lambda = 0.5$, $S = 3\ \mu_B$, $h_0 = 0$, and $J = 0.45$ eV/μ_B^2. Inset: Magnetization as a function of the size of nanocubes if the edge effect and finite ferromagnetic thickness is considered. The width of the edges is $w = 50$ nm, the ferromagnetic thickness is $\eta = 7.2$ nm, and $U = 2.5$ eV.

To demonstrate the application to spintronic devices, a SQUID magnetometer equipped with an optical fiber and light pipe is utilized. The samples are irradiated with a 425 nm laser (100 mW). The magnetization curves under light irradiation are shown in Figure 3a (blue line). After irradiation, the magnetization curve shows no hysteretic behavior, as shown by the solid triangles. Based on the photogenerated carriers, it is demonstrated that the degree of ferromagnetic spin exchange on the surface of β-$FeSi_2$ nanocubes can be controlled under light irradiation and a small change in the carrier number influences the magnetic properties.[43] When we turn the light off, the magnetization curve is nearly the same as that before light irradiation (Figure 3a, red line). This experimental result clearly shows that the change in magnetization is purely electronic, and is not accompanied by any photo- and/or heat-induced structural or chemical changes. The excitation by light drives electrons out of the itinerant subbands, leading to the disappearance of the ferromagnetism.

CONCLUSION

Crystalline semiconducting β-$FeSi_2$ nanocubes show strong room-temperature ferromagnetism suggesting a promising way to induce strong magnetism from nonmagnetic semiconductors by simply exposing specific crystal facets. The coexistence of surface ferromagnetism, polarized surface bands in the energy gap, and semiconductor characteristics (Figure S9) in the same nanocubes provides an ideal platform to electrically and optically control magnetism and also conversely, magnetically control the electrical and optical properties. The semiconducting β-$FeSi_2$ nanocubes may be used in elementary magnetic storage units and magneto-optic components suitable for silicon-based spintronics applications.

EXPERIMENTAL SECTION

Materials. The crystalline β-$FeSi_2$ nanocubes were synthesized in a horizontal two-zone pipe furnace by chemical vapor deposition (CVD) (Figure S1). Five-hundredths of a gram of anhydrous $FeCl_2$ powders (99.5% from Alfa Aesar) as the precursors was placed on an alumina boat (the yellow rectangle) and the loaded boat together with a rectangular Si substrate (1 cm × 1 cm, the blue square) was placed in a shorter and smaller diameter quartz tube with a diameter of 2.5 cm (tube 1). The distance between the boat and Si substrate was 32 cm. The small-diameter quartz tube was placed in a large quartz tube with a diameter of 6 cm (tube 2) constituting the precursors and Si substrate in the upstream and downstream zones, respectively. The Si (100) substrates were cleaned by 1 wt %-buffered HF. The quartz tube was evacuated to a pressure of 1×10^{-3} Pa by a mechanical pump and turbomolecular pumps and then purged with Ar (99.99%). In the synthesis, Ar (99.99%) was introduced as a carrier gas at a constant gas flow of 100 SCCM (cubic centimeter per minute). The upstream zone was heated from room temperature to 600 °C and the downstream zone was heated to 800 °C in 20 min. When the furnace reached the set temperature, the $FeCl_2$ precursors produced vapor-phase $FeCl_2$ that was mixed with flowing Ar to react with the Si substrate. The β-$FeSi_2$ nanocubes were collected from the Si substrates. The reaction at atmospheric pressure proceeded for 2 h at a constant Ar flow of 100 SCCM and afterward, the furnace was cooled to room temperature slowly.

Characterization. The morphology of the β-$FeSi_2$ nanocubes was examined by field-emission scanning electron microscopy (FE-SEM, Hitachi S4800). The microstructure and chemical composition were determined by using X-ray powder diffraction (XRD, Philips, Xpert), X-ray photoelectron spectroscopy (XPS, PHI5000 VersaProbe), and high-resolution transmission electron microscopy (HR-TEM, JEOL-2100). The samples were put in ethanol and ultrasonically treated at a frequency and power of 40 kHz and 150 W, respectively. Several drops of the suspensions after the ultrasonic treatment were put on a copper mesh initially coated with a thin layer of carbon. The magnetic properties were determined by SQUID and VSM. An atomic force microscope (AFM, Digital Instruments, Nanoscope IIIa) was utilized to measure the surface topography and magnetic domains using the MFM mode. In the MFM experiments, the sample was in the initial state without any magnetic treatment. The AFM tips were provided by Nano World Ltd. Co (Type MESP). The cantilever oscillating frequency was 60−100 Hz and module of elasticity was 1−5 N/m. The tapping mode was adopted to obtain the magnetic micrographs and the height was 100 nm. The Mössbauer spectra were obtained with a radioactive source of ^{57}Fe in the Rh matrix at room temperature in a transmission configuration at constant acceleration and the spectrometer was calibrated by using the room-temperature spectrum of an α-Fe foil.

ASSOCIATED CONTENT

Supporting Information

The Supporting Information is available free of charge on the ACS Publications website at DOI: 10.1021/jacs.5b06507.

Figures S1−S9, details regarding the growth process and mechanism of β-$FeSi_2$ nanocubes and the first-principles calculation, calculated temperature and size dependence of magnetization (PDF)

AUTHOR INFORMATION

Corresponding Author

*hkxlwu@nju.edu.cn

Notes

The authors declare no competing financial interest.

ACKNOWLEDGMENTS

This work was jointly supported by National Basic Research Programs of China (2011CB922102, 2014CB339800, and 2013CB932901), National Natural Science Foundation of China (21203098 and 11374141).

REFERENCES

(1) Žutić, I.; Fabian, J.; Das Sarma, S. *Rev. Mod. Phys.* **2004**, *76*, 323.
(2) Wolf, S. A.; Awschalom, D. D.; Buhrman, R. A.; Daughton, J. M.; von Molnár, S.; Roukes, M. L.; Chtchelkanova, A. Y.; Treger, D. M. *Science* **2001**, *294*, 1488.
(3) Ando, K. *Science* **2006**, *312*, 1883.
(4) Dietl, T. *Nat. Mater.* **2010**, *9*, 965.

DOI: 10.1021/jacs.5b06507
J. Am. Chem. Soc. 2015, 137, 11419−11424

(5) Wang, Q.; Sun, Q.; Chen, G.; Kawazoe, Y.; Jena, P. *Phys. Rev. B: Condens. Matter Mater. Phys.* **2008**, *77*, 205411.
(6) Chen, S. Y.; Lu, Y. H.; Huang, T. W.; Yan, D. C.; Dong, C. L. *J. Phys. Chem. C* **2010**, *114*, 19576.
(7) Garcia, M. A.; Merino, J. M.; Fernández Pinel, E.; Quesada, A.; de la Venta, J.; Ruíz González, M. L.; Castro, G. R.; Crespo, P.; Llopis, J.; González-Calbet, J. M.; Hernando, A. *Nano Lett.* **2007**, *7*, 1489.
(8) Zhang, J. H.; Xiong, S. J.; Wu, X. L.; Thurber, A.; Jones, M.; Gu, M.; Pan, Z. D.; Tenne, D. A.; Hanna, C. B.; Du, Y. W.; Punnoose, A. *Phys. Rev. B: Condens. Matter Mater. Phys.* **2013**, *88*, 085437.
(9) Ohno, H.; Chiba, D.; Matsukura, F.; Omiya, T.; Abe, E.; Dietl, T.; Ohno, Y.; Ohtani, K. *Nature* **2000**, *408*, 944.
(10) Korenev, V. L.; Akimov, I. A.; Zaitsev, S. V.; Sapega, V. F.; Langer, L.; Yakovlev, D. R.; Danilov, Yu. A.; Bayer, M. *Nat. Commun.* **2012**, *3*, 959.
(11) Leong, D.; Harry, M.; Reeson, K. J.; Homewood, K. P. *Nature* **1997**, *387*, 686.
(12) Martinelli, L.; Grilli, E.; Migas, D. B.; Miglio, L.; Marabelli, F.; Soci, C.; Geddo, M.; Grimaldi, M. G.; Spinella, C. *Phys. Rev. B: Condens. Matter Mater. Phys.* **2002**, *66*, 085320.
(13) Wadia, C.; Alivisatos, A. P.; Kammen, D. M. *Environ. Sci. Technol.* **2009**, *43*, 2072.
(14) Dalapati, G. K.; Liew, S. L.; Wong, A. S. W.; Chai, Y.; Chiam, S. Y.; Chi, D. Z. *Appl. Phys. Lett.* **2011**, *98*, 013507.
(15) Grimaldi, M. G.; Bongiorno, C.; Spinella, C.; Grilli, E.; Martinelli, L.; Gemelli, M.; Migas, D. B.; Miglio, L.; Fanciulli, M. *Phys. Rev. B: Condens. Matter Mater. Phys.* **2002**, *66*, 085319.
(16) Suemasu, T.; Negishi, Y.; Takakura, K.; Hasegawa, F.; Chikyow, T. *Appl. Phys. Lett.* **2001**, *79*, 1804.
(17) Yasui, N.; Horie, R.; Ohashi, Y.; Tanji, K.; Den, T. *Adv. Mater.* **2007**, *19*, 2797.
(18) Rizzi, A.; Rösen, B. N. E.; Freundt, D.; Dieker, Ch.; Lüth, H.; Gerthsen, D. *Phys. Rev. B: Condens. Matter Mater. Phys.* **1995**, *51*, 17780.
(19) Hung, S. W.; Yeh, P. H.; Chu, L. W.; Chen, C. D.; Chou, L. J.; Wu, Y. J.; Chen, L. J. *J. Mater. Chem.* **2011**, *21*, 5704.
(20) Bywalez, R.; Orthner, H.; Mehmedovic, E.; Imlau, R.; Kovacs, A.; Luysberg, M.; Wiggers, H. *J. Nanopart. Res.* **2013**, *15*, 1878.
(21) Dahal, N.; Chikan, V. *Chem. Mater.* **2010**, *22*, 2892.
(22) Birkholz, U.; Frühauf, A. *Phys. Status Solidi B* **1969**, *34*, K181.
(23) Valassiades, O.; Dimitriadis, C. A.; Werner, J. H. *J. Appl. Phys.* **1991**, *70*, 890.
(24) Arushanov, E.; Bucher, E.; Kloc, Ch.; Kulikova, O.; Kulyuk, L.; Siminel, A. *Phys. Rev. B: Condens. Matter Mater. Phys.* **1995**, *52*, 20.
(25) Arushanov, E.; Kloc, Ch.; Bucher, E. *Phys. Rev. B: Condens. Matter Mater. Phys.* **1994**, *50*, 2653.
(26) Arushanov, E.; Respaud, M.; Broto, J. M.; Kloc, Ch.; Leotin, J.; Bucher, E. *Phys. Rev. B: Condens. Matter Mater. Phys.* **1996**, *53*, 5108.
(27) Arushanov, E.; Behr, G.; Schumann, J. *Thin Solid Films* **2004**, *461*, 148.
(28) Peng, Z. L.; Liang, S. *Chin. Phys. Lett.* **2008**, *25*, 4113.
(29) Chen, Y. Y.; Lee, P. C.; Tsai, C. B.; Neeleshwar, S.; Wang, C. R.; Ho, J. C.; Hamdeh, H. H. *Appl. Phys. Lett.* **2007**, *91*, 251907.
(30) Singh, D. J.; Parker, D. *Sci. Rep.* **2013**, *3*, 3517.
(31) Seo, K.; Lee, S.; Jo, Y.; Jung, M. H.; Kim, J.; Churchill, D. G.; Kim, B. *J. Phys. Chem. C* **2009**, *113*, 6902.
(32) Sonoda, S.; Shimizu, S.; Sasaki, T.; Yamamoto, Y.; Hori, H. *J. Cryst. Growth* **2002**, *237*, 1358.
(33) Fanciulli, M.; Rosenblad, C.; Weyer, G.; Svane, A.; Christensen, N. E.; Von Känel, H. *Phys. Rev. Lett.* **1995**, *75*, 1642.
(34) Aigner, W.; Niesar, S.; Mehmedovic, E.; Opel, M.; Wagner, F. E.; Wiggers, H.; Stutzmann, M. *J. Appl. Phys.* **2013**, *114*, 134308.
(35) McIntyre, N. S.; Zetaruk, D. G. *Anal. Chem.* **1977**, *49*, 1521.
(36) Anwar, M.; Hogarth, C. A.; Bulpett, R. *J. Mater. Sci.* **1990**, *25*, 1784.
(37) Taylor, J. A.; Lancaster, G. M.; Ignatiev, A.; Rabalais, J. W. *J. Chem. Phys.* **1978**, *68*, 1776.
(38) Bird, C. F.; Bowler, D. R. *Surf. Sci.* **2003**, *531*, L351.
(39) Sheka, E. F.; Nikitina, E. A.; Zayets, V. A. *Surf. Sci.* **2003**, *532–535*, 754.
(40) Seo, K.; Varadwaj, K. S. K.; Mohanty, P.; Lee, S.; Jo, Y.; Jung, M. H.; Kim, J.; Kim, B. *Nano Lett.* **2007**, *7*, 1240.
(41) Hung, S. W.; Wang, T. T. J.; Chu, L. W.; Chen, L. J. *J. Phys. Chem. C* **2011**, *115*, 15592.
(42) Huang, X. H.; Li, L.; Luo, X.; Zhu, X. G.; Li, G. H. *J. Phys. Chem. C* **2008**, *112*, 1468.
(43) Koshihara, S.; Oiwa, A.; Hirasawa, M.; Katsumoto, S.; Iye, Y.; Urano, C.; Takagi, H.; Munekata, H. *Phys. Rev. Lett.* **1997**, *78*, 4617.

DOI: 10.1021/jacs.5b06507
J. Am. Chem. Soc. 2015, 137, 11419–11424